



Improving electrocatalytic activity of iridium for hydrogen evolution at high current densities above 1000 mA cm^{-2}

Peng Jiang^{a,1}, Hao Huang^{a,1}, Jiefeng Diao^a, Shipeng Gong^a, Shi Chen^a, Jian Lu^a, Changlai Wang^a, Zhijuan Sun^a, Guoliang Xia^a, Kang Yang^a, Yang Yang^a, Lingzhi Wei^c, Qianwang Chen^{a,b,*}

^a Hefei National Laboratory for Physical Science at Microscale, Department of Materials Science & Engineering & Collaborative Innovation Center of Suzhou Nano Science and Technology, University of Science and Technology of China, Hefei 230026, China

^b The Anhui Key Laboratory of Condensed Matter Physics at Extreme Conditions, High Magnetic Field Laboratory, Hefei Institutes of Physical Science, Chinese Academy of Sciences, Hefei 230031, China

^c Institute of Physical Science and Information Technology, Anhui University, Hefei 230601, China

ARTICLE INFO

Keywords:

Metal-organic frameworks
Electrocatalysis
IrFe nanoalloys
High current density
Modulated electronic structure.

ABSTRACT

The exploration of electrocatalysts with high activity and durability for hydrogen evolution reaction (HER) at extremely high current densities above 500 mA cm^{-2} in alkaline media is the basis for large-scale industrial applications. Plain Ir possesses optimum performance for OER in alkaline electrolytes but presents a noticeable underperforming HER activity. Herein, the strategy by pyrolyzing Ir-modified metal-organic frameworks (MOFs) precursors has been employed in designing electrocatalysts consisting of IrFe nanoalloys supported on N-doped carbon layers. The catalyst requires a small overpotential of 105 mV to deliver a current density of 100 mA cm^{-2} in basic media, which surpasses that of commercial Ir/C and Pt/C benchmarks. Particularly, the catalyst also exhibits an extraordinary performance with low overpotential of only 850 mV at 1000 mA cm^{-2} . The extraordinary performance originates from superior conductivity, the modulated electronic structure and large specific surface area.

1. Introduction

The everlasting but formidable challenge confronting the future on-board fuel cells lies in the lack of cheap alternatives to Pt-based electrocatalysts to drive the scalable production of hydrogen with zero-emission [1–3]. Despite the fact that superior progress has been achieved, there is a rather limited improvement of performance towards HER in overpotential and stability due to the intrinsically sluggish kinetics. Moreover, the properties of most candidate materials can't approach those of Pt-based catalysts benchmarks in respect of electricity-to-hydrogen conversion efficiency at high current density over a wide pH range [4–6].

Generally, the overpotential to drive a 10 mA cm^{-2} current density is employed to assess the HER performance of one catalyst. In other words, the larger the current density at a fixed overpotential, the higher the electricity-to-hydrogen-energy efficiency [7,8]. It can be anticipated that a larger amount of hydrogen can be produced by an excellent catalyst compared to the common catalyst counterpart under otherwise identical conditions. The Tafel slope extracted from the linear portion

of the Tafel plot is a good descriptor to mirror the nature of the reaction kinetics. Normally a relatively small Tafel slope value indicates that the current density increases fast with rising overpotential [9]. To date, a host of Pt-free catalysts have received extensive attention for their superior HER catalytic activities operated at small current densities (e.g., at about 10 mA cm^{-2}). A biphasic Ni-Mo-N material with high efficiency and good stability is developed and confirmed as an alternative to commercial Pt/C catalyst [10]. It is also reported by Mu and co-authors that the RuP₂-embedded in N, P dual-doped carbon cages exhibits Pt-like HER performance at 10 mA cm^{-2} [5]. Even so, the Tafel slopes of them are far behind the precious metal catalyst Pt. It means that the current reported candidates can't efficiently afford a large current densities especially in the order of 1000 mA cm^{-2} in practical large-scale applications compared with Pt-based catalysts counterparts. Therefore, the ultimate goal of catalyst design is to develop budget catalysts with enhanced HER efficiency for practical water electrolysis [11].

On the other hand, the commercialization of alkaline water electrolyzers is still somewhat bottlenecked by insurmountable demerits

* Corresponding author.

E-mail address: cqw@ustc.edu.cn (Q. Chen).

¹ Peng Jiang and Hao Huang contributed equally.

associated with the lack of ideal electrocatalyst for H_2 -production at high current densities above 500 mA cm^{-2} in basic media [10,12]. It is well known that the sluggish kinetics of counter electrode catalysts toward oxygen evolution reaction (OER) which involving in four-electron transfer steps greatly impede the widespread implementation of these alternative catalysts. Thus, it is of paramount importance to develop HER electrocatalysts on the basis of the current commercial alkaline OER catalysts to meet the commercial requirements of H_2 -production process for current densities in the order of 1000 mA cm^{-2} [11]. Given the widespread application prospect on current alkaline electrolysis technology, it is highly desirable to develop high-activity Pt-free catalysts in alkaline electrolytes [13–17].

Traditionally, Iridium is obviously considered as the benchmark for OER under both acidic and basic media [18]. Efficient as it is, the potential for hydrogen generation of Ir remains to be developed. Particularly, Guo and co-workers synthesized porous hollow CoNiIr nanocrystals and demonstrated their attractive activities for both OER and HER in acidic electrolytes [19]. However, there is barely coverage of their underlying HER properties in basic media in previous studies [20]. For good measure, the creation of Ir-based materials could circumvent the inevitable variation of proton concentration during the course of hydrogen evolution, and consequently maintain the initial energy-conversion efficiency of water electrolysis. Motivated by these considerations, the development or boost of HER performance of Ir-based materials at high current densities in basic media can be a feasible practice and deserves further exploration [21].

Previous experimental studies, in combination with calculation results, illustrate that the catalytic activity, especially at large current density, correlates with surface electronic structure, active-site density and reaction kinetics [8,11,21–23]. It is well known that alloying noble metals with late transition metals (TMs) is a major trend to maneuver the catalytic behavior of catalyst with dosage of noble metal down [24]. The filling of noble metal d -band accompanying a downshift in the d -band center energy is originated from the difference in electronegativity between precious metal (e.g., Ir) and TMs (e.g., Fe), which producing a favorable electronic structure that effectively facilitates performance improvement [25]. Furthermore, metal-organic frameworks (MOFs) with periodically porous and hybrid structures are often used as precursors or templates to fabricate nanostructured materials with large specific surface area, which is good for the exposure of active sites [26].

In this work, a MOFs-assisted protocol is employed to develop Ir-based electrocatalysts consisting of IrFe nanoalloys supported on N-doped carbon layers (IrFe/NC) for efficient hydrogen generation under both acid and alkaline conditions. Particularly, the catalytic capacity in basic media is more superior to that of commercial Pt/C. The excellent catalytic activities of the target IrFe/NC hybrid materials originate from the modulated surface electronic structures induced by the introduction of iron atoms.

2. Results and discussion

The overall synthetic route to fabricate IrFe nanoalloys loaded on N-doped carbon layers is illustrated in Fig. 1a. We take advantage of one-step pyrolysis of Ir-modified Fe-based MOFs strategy to synthesize the desired hybrids. The scanning electron microscopy (SEM) and transmission electron microscopy (TEM) images illustrated in Figs. 1b, c and S1 display the sheetlike feature of carbon substrates with rough surface because of the decomposition of the framework and subsequently etching with acidic solution [27]. The statistical analysis from HRTEM images also clearly shows the mean diameter of IrFe nanoparticles is 1.85 nm (Figure S2). According to the N_2 adsorption-desorption isotherm shown in Figure S3a, the specific surface area of IrFe/NC is calculated to be $457.2 \text{ m}^2 \text{ g}^{-1}$. The strong and narrow size distribution centered at 0.634 nm in Figure S3b is attributed to the existence of a host of nanopores, while the weak and wide pore-size distribution

centered at 8.97 nm can be ascribed to some larger pores owing to the connection of small pores (inset of Figure S3b).²⁶ These results are in good line with the above morphology observations. The microscopic phase information of the final product is confirmed by high-resolution transmission electron microscopy (HRTEM) in Fig. 1d. The lattice fringes with interspace of 0.218 nm and 0.19 nm are close to but smaller than the (111) ($d = 0.221 \text{ nm}$) and (200) ($d = 0.192 \text{ nm}$) lattice planes of pure Ir phase, respectively [24]. Besides, the angle between lattice fringes is about 54.5° , which corresponds well to interfacial angle of these planes. The energy dispersive spectroscopy (EDS) mapping results in Fig. 1e–h show that Ir and Fe elements are uniformly distributed over the entire N-doped carbon network, further revealing the formation of IrFe alloys supported on N-doped porous carbon sheets.

The bare characteristic also demonstrates that the IrFe nanoparticles are not encapsulated by carbon sheets. However, isolated single Fe-N_x moieties embedded on N-doped carbon [28,29], nitrogen implanted carbon nanotubes [30] or N-doped graphene coated Fe species [31] can be obtained by calcinating other Fe-based zeolitic imidazolate frameworks. The sharp distinction of final structures after simple thermolysis of MOFs precursors is governed by a combination of the metal-ligand coordination environment [32], the metal element contents, reduction potential of metal atoms and the pyrolysis atmosphere [33].

The phase and crystallography of the as-synthesized samples were characterized by scanning TEM (STEM), EDS measurements and X-ray diffraction. Notably, the element mappings (Figure S4 and S5) and line-scanning profile (Figure S5g–h) results demonstrate that the nanoalloys are encapsulated by Fe nanoparticles. Also, there exist many metallic Fe nanoparticles. Compared to the two characteristic diffraction peaks of Fe, the diffraction angles of the sample annealed in Ar/ H_2 atmosphere have moved in low-angle region owing to the formation of alloy in Figure S6. After the acid etching, the redundant Fe species were removed while the three diffraction peaks of the resulting precipitate in Fig. 2a were ascribed to (111), (200), and (220) of metallic Ir. Besides, the diffraction angles of IrFe/NC were close to but a little higher than that of monometallic Ir (JCPDS 87-0715), indicating the contracted lattice distance of Ir in response to the successfully permeation of Fe. Remarkably, the broadened peaks probably signify the existence of nanocrystallites with small size. X-ray absorption near-edge structure (XANES) was performed to probe the coordination and bonding environments of atoms. The L_{3-2} region ($2p_{3/2} \rightarrow 3d$ transitions) of Fe L -edge XANES spectrum for IrFe/NC is dominated by a main peak about 707.8 eV in Fig. 2b, which situated between Fe powder (707 eV) and Fe-Pc (Hemin, 708.47 eV) [34]. It can conclude that the valence state of Fe in as-made products is mainly located between Fe (0) and Fe (II), namely the oxidized Fe species. The valence of Fe is influenced by the interaction between Ir and Fe, the strong interaction between N dopants (such as Fe-N_x moieties) and the adsorption of Fe species from the solution.

X-ray photoelectron spectroscopy (XPS) was conducted as a strong tool to identify the nature of the interaction between Ir and Fe. (Figure S7 and Table S1) The mass percentage of Ir for IrFe/NC was determined to be 25.09% according to the XPS results. Compared to two strong peaks of commercial Ir powder and Ir/NC sample in Fig. 2c, Ir 4f peaks for IrFe/NC shifted to lower binding energies, which indicated Ir accepts electrons. The peak fitting of Fe 2p survey in Fig. 2d showed that there exist three states (0, +2 and +3) for Fe in IrFe/NC, confirming the changed Fe 3d-band electron density. The above mentioned XPS results implied that the negative shifts of Ir peaks stemmed from the electrons transferred from Fe to Ir [35], which was in good agreement with XANES results mentioned above. Additionally, the deconvolution of the N 1s spectra in Figure S7b indicated three individual chemical states of nitrogen species: pyridinic N (398.5 eV), pyrrolic N (400.2 eV), and quaternary N (401.7 eV), revealing the formation of nitrogen-doped carbon after post-treatment [26]. The I_p/I_g band intensity ratio of IrFe/NC calculated from Raman spectroscopy (Figure S8) is 0.76, indicating the existence of abundant defects. Additionally, the

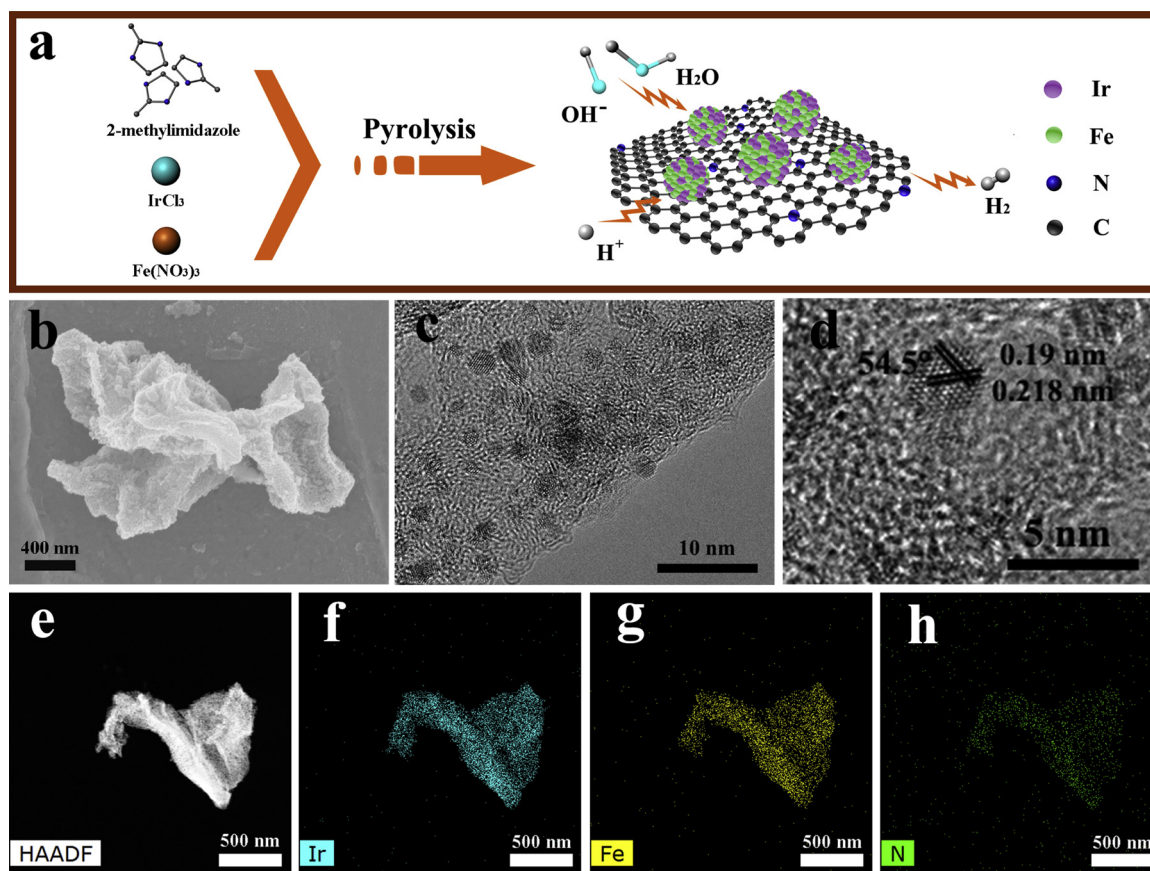


Fig. 1. Schematic illustration of model and synthetic process and characterization of IrFe/NC hybrid. (a) Synthetic route for IrFe nanoalloys loaded on N-doped carbon layers. (b,c) Representative SEM (b) and TEM images (c) of IrFe/NC, respectively. (d) HRTEM images of IrFe/NC. (e–h) HAADF image and corresponding EDS elemental mapping of Ir, Fe and N, respectively.

broadened but weak 2D band demonstrates that the carbon bases are graphene with several layers [36].

Electrochemical measurements were performed in a three-electrode configuration to verify whether the IrFe/NC catalyst possesses an enhanced HER capacity as compared to Ir counterpart in both acidic and basic electrolytes. The contents of Ir and Fe for IrFe/NC were determined to be 23.74 wt.% and 4.69 wt.%, respectively. Fig. 3a showed the polarization curves of IrFe/NC and Fe/NC samples, along with that of the state-of-the-art Ir/C and Pt/C catalyst for comparison. It is obvious that Fe/NC sample displayed negligible or poor HER performance, whereas IrFe/NC catalyst required the smallest overpotential (η) of 101 mV to deliver a current density of 100 mA cm^{-2} , which surpasses that of commercial Ir/C and Pt/C benchmarks. Interestingly, Pt/C produced a current density of 10 mA cm^{-2} at a small η of 37 mV, while IrFe/NC exhibited a relative larger η of 41 mV to achieve the same current density (inset of 3a). This unique phenomenon indicated that the cathodic current of Pt/C enhanced much slower with rising overpotential than that of IrFe/NC, namely, the later outperformed the former for large η with rapidly increasing cathodic current, which can be reflected by the Tafel slope. It is worth noting that Tafel slope is employed as an intrinsic parameter for disclosing kinetic-level insights into the rate determining step of HER. Among them, Ir/C gives a slope of 43 mV dec^{-1} , suggesting the reaction undergoes the Volmer–Heyrovsky mechanism, in which the desorption Heyrovsky step is rate-limiting. In line with the above results, IrFe/NC displays a smaller Tafel slope at 22 mV dec^{-1} than Pt/C benchmark (29 mV dec^{-1}). It is well known that a lower Tafel slope mirrors that the current gain is more rapidly with rising potential [7]. In view of all the above electrochemical results, we can draw the conclusion that IrFe/NC catalyst with prominent activities outperforms the Pt/C catalyst for sufficiently high

overpotentials or large current densities in practical industrial application. Besides, Ir/NC sample exhibits a relative larger overpotential to achieve the same current density compared to IrFe/NC counterpart in acidic electrolytes in Figure S9, indicating the promotion effect of Fe.

The interface reactions and electrode kinetics of the catalysts in the HER can be further manifested by electrochemical impedance spectroscopy (EIS). The plot is composed of a semicircle at high-frequency regions and a vertical line at low-frequency regions in Figure S10. The small diameter of the semicircle indicates the low charge-transfer impedance. The catalytic durability is also a critical criterion for evaluating efficient HER catalysts. Accelerated degradation tests with long-term potential cycling (cyclic voltammetry sweeps) were performed on the electrode. There was no obvious degradation for IrFe/NC after 20,000 cycles to sustain a current density of 100 mA cm^{-2} . (Fig. 3c) The effect current density on metal dissolving has also been investigated in Figure S11–S13 and Table S2, those results also indicated its robust structure [37]. The stability was also evaluated by the time-dependent chronopotentiometry. Only a little deterioration of catalytic currents can be found after the prolonged electrolysis at a constant potential (100 mV) over 10 h (inset of Fig. 3c). The fluctuation can be ascribed to the accumulation and desorption of hydrogen during electrolysis reaction. IrFe/NC catalyst loaded on carbon paper was also employed as the working electrode to determine the stability. Obviously, the overpotential exhibits negligible change over 10 h of testing at 100 mA cm^{-2} in Figure S14. These results demonstrated the superior long-term stability of IrFe/NC under the experimental conditions. The electrochemical production of H₂ on the cathode in an H-type electrolytic cell was collected and identified quantitatively by gas chromatography (GC). The specific Faradaic efficiency was measured by galvanostatic electrolysis at 200 mA cm^{-2} for 60 min. Obviously, the IrFe/NC

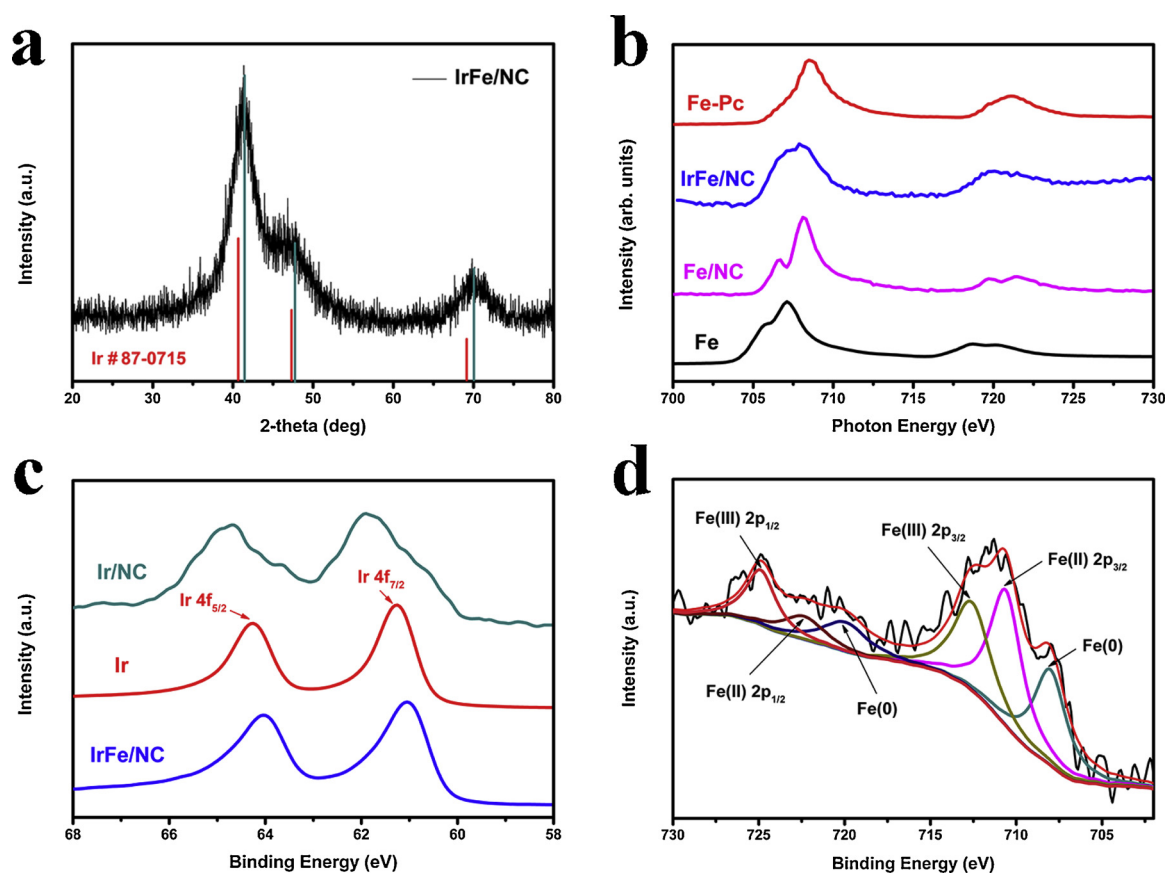


Fig. 2. Structural analysis of IrFe/NC hybrids. XAF spectra of IrFe/NC, Fe, Fe/NC and Fe-Pc, respectively, (c) The Ir 4f XPS spectra of IrFe/NC, Ir/NC and commercial Ir powder, (d) The Fe 2p XPS spectrum of IrFe/NC sample.

sample displayed about 100% Faradaic yield in 0.5 M H_2SO_4 in the whole test process.

The main difficulties confronting the commercialization of alkaline electrolyzers lie in that the HER activities of most reported alkaline OER electrocatalysts are still far inferior to commercial available HER catalysts. Thus, activating and optimizing the underlying HER activity of the accessible basic oxygen evolution catalysts will exert direct influence on alkaline electrolyzers and electrolysis technology [38–40]. The HER performance of IrFe/NC catalyst is also tested in 1 M KOH electrolytes. As shown in Fig. 4a, neither 20% Ir/C nor 40% Pt/C exhibits better HER activity than the as-synthesized IrFe/NC sample. Comparison of overpotentials at 10, 100 and 200 mA cm^{-2} for IrFe/NC, Ir/C and Pt/C is listed in Fig. 4b. Specifically, IrFe/NC sample needs only 22 mV to reach a current density of 10 mA cm^{-2} , outperforming the other catalysts including 40% Pt/C. The trend in the overpotentials to drive a current density of 100 mA cm^{-2} is ranked in the following sequence: IrFe/NC (105 mV) < Pt/C (264 mV) < Ir/C (330 mV). Such activities are among the best reported as compared with most recent reported catalysts including Ru-based materials (Table S3). Additionally, the IrFe/NC catalyst also displayed an enhanced HER activity in alkaline solution relative to Ir/NC catalyst in Figure S15, indicating the promotion effect of Fe. Since the evolution of hydrogen in practical industrial applications requires a large order of magnitude of current densities, it is of paramount importance to probe its activity at a larger current (such as 1000 mA cm^{-2}). At 1000 mA cm^{-2} , the IrFe/NC and Pt/C require overpotentials of about 0.85 V and 1.17 V, respectively. In other words, there exists a large gap of 300 mV between the two catalysts. Moreover, the calculated Tafel slope of IrFe/NC is only 30 mV/dec, lowering than that of Pt/C and Ir/C in the same region. (Figure S16)

As depicted in Fig. 4d, the reliable electrochemical durability of

IrFe/NC was also conducted by accelerated durability test. Only small degeneration of current density after 5000 and 10,000 continuous potential cycles can be found, indicating the strong stabilities of IrFe/NC sample. According to the results revealed in Fig. 4e and 4f, IrFe/NC exhibits a near 100% Faradaic yield and an ascendant stability during the Faraday efficiency testing process.

Density functional theory (DFT) calculations were carried out to better understand the origin of the excellent activity of the IrFe alloy for HER. The details of the calculation can be found in the Supporting Information. In general, the Gibbs free energy of H^* absorption (ΔG_{H^*}) is one of the key descriptors in theoretical prediction of the activity for HER. A good catalyst of the HER should have a moderate free energy (ΔG_{H^*} close to 0) to compromise the reaction barriers of the adsorption and desorption steps.

Here, we calculated ΔG_{H^*} of different models, including IrFe alloy, pure Ir, pure Pt, pure graphene as well as graphene doped with graphitic nitrogen according to the XPS results. (Figure S17–S20) The optimized adsorption structures are shown in Fig. 5a. For IrFe alloy, pure Ir and pure Pt, the active adsorption site for H^* is the top site of the surface. And for N-doped graphene, the active adsorption site for H^* is the C atom next to the doping N atom in graphene, which is consistent with previous work. As illustrated in Fig. 5b and Table S4–S5, the pristine graphene exhibited a positive and large ΔG_{H^*} of 2.51 eV, indicating negligible adsorption ability of H^* . After introducing an N atom into graphene, ΔG_{H^*} on graphene remarkably decreases. However, the ΔG_{H^*} values of IrFe alloy (200), pure Ir (200) and pure Pt (111) are far more closer to zero compared to graphene and N-doped graphene, which indicates that precious metal in the synthesized samples is the main factor to improve the activity for HER. We can also see that the ΔG_{H^*} value of IrFe alloy (−0.25 eV) is closer than the value of pure Ir (−0.33 eV), indicating that the introduction of an iron atom into

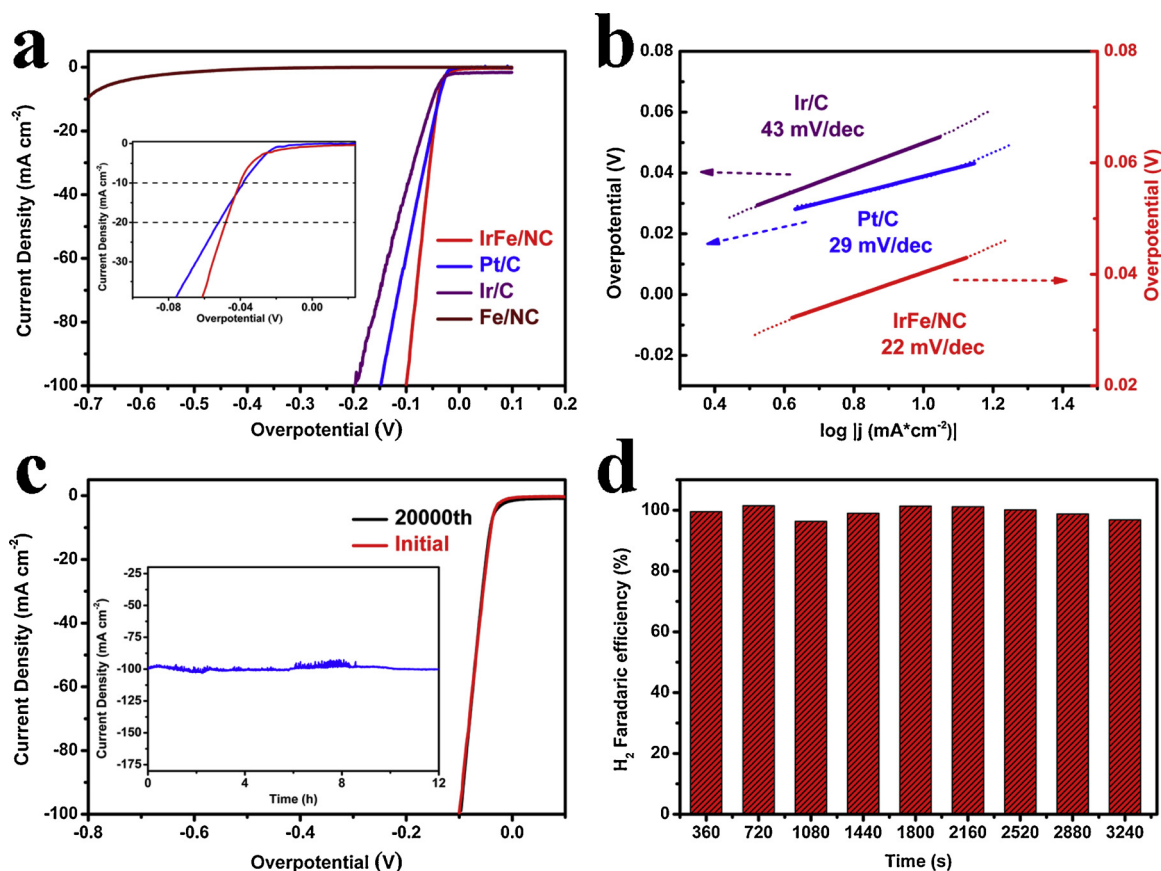


Fig. 3. HER performance of catalysts in N₂ saturated 0.5 M H₂SO₄ solution. (a) Polarization curves of IrFe/NC, Pt/C, Ir/C and Fe/NC in 0.5 M H₂SO₄ solutions, inset of (a): Comparison between IrFe/NC (red) and Pt/C (blue) in the range of 0–40 mA cm⁻² current density in (a), (b) Corresponding Tafel plots for IrFe/NC, Pt/C and Ir/C, (c) LSV curves for IrFe/NC before and after 20,000 cycles in 0.5 M H₂SO₄, inset of (c) the chronoamperometric (i–t) operated at a fixed overpotential of 100 mV, (d) Specific Faradaic efficiency for electrochemical production of H₂ measured on IrFe/NC catalyst at 200 mA cm⁻² in 0.5 M H₂SO₄. (For interpretation of the references to colour in this figure legend, the reader is referred to the web version of this article).

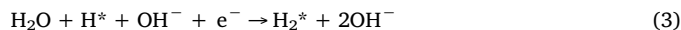
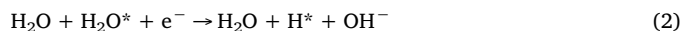
pure Ir can enhance the electrocatalytic performance. The calculation result is also consistent with the experimental results. Additionally, the Ir (111) model is also concerned about in our DFT calculations in Figure S21, and the result is consistent with the Ir (200) model. According to the free energy diagram in Figure S22, we can also see that the ΔG_{H^*} value of IrFe alloy (-0.05 eV) is closer to zero than the value of Ir (111) surface (-0.1 eV), also indicating that the introduction of an iron atom into pure Ir can enhance the electrocatalytic performance.

To gain further understand into the high electrocatalytic activity of the IrFe alloy, we performed Bader charge calculations. As illustrated in Supplementary Figure S23 and Table S6, the exact number of transferred electron was calculated using bader charge analysis. The number of interatomic-polarized charges is not much altered by the introduction of an iron atom. Meanwhile, the Ir atoms near the introduced iron atom can accumulate more electrons to generate highly active sites. The Ir atom that offers active adsorption site for H⁺ shows the larger number of electrons (9.1103 e⁻) with the introduction of an iron atom compared to pure Ir (9.0072 e⁻) [25]. Therefore, the ΔG_{H^*} of IrFe alloy is lower than that of pure Ir. This result indicates that introducing an iron atom into pure Ir can enhance the electrocatalytic activity due to electrons accumulation around the Ir atom.

The electronic structure is another key parameter to electrocatalysis. To reveal the electronic structures, we further calculate the Partial Density of States (PDOS) of Ir atom *d* orbitals in the model of IrFe alloy and pure Ir. As illustrated in Fig. 5c and 5d, there is no clear information we can obtain from the PDOS distributions. Therefore, to catch on more details about the electronic structures of the Ir *d* orbitals, we average the energy levels of all the *d* electrons in the Ir atom and get

the values of *d*-band centers. It's known that too high or too low position of the *d*-band center relative to the Fermi level would lead to the reduction of the electrocatalytic activity. As listed in Table S7, the position of *d*-band center shifts from -3.117 eV to -3.124 eV, which is far away from the Fermi level, after Fe doping. According to previous work, the lower in energy the *d* states are, the weaker the bonds that are formed between adsorbed hydrogen atoms and the surface [41]. Through the free energy diagram, the strong interaction between hydrogen atoms and the Ir surface would hinder the HER performance. As a result, proper downshift of *d*-band center to the Fermi level is beneficial for improving the HER performance, indicating the electrocatalytic activity can be enhanced with the introduction of an iron atom.

In alkaline media, the HER pathway could be summarized by the following four elementary steps according to previous work.



The optimized structures of basic HER intermediate states H₂O*, H₂* are shown in Figure S24. To investigate the energy process along the HER pathway, we calculated the Gibbs free energy of four elementary steps of IrFe alloy and pure Ir. More calculation details about the free energy can be found in supporting information, and the results can be concluded as the free energy diagram illustrated in Fig. 6. As

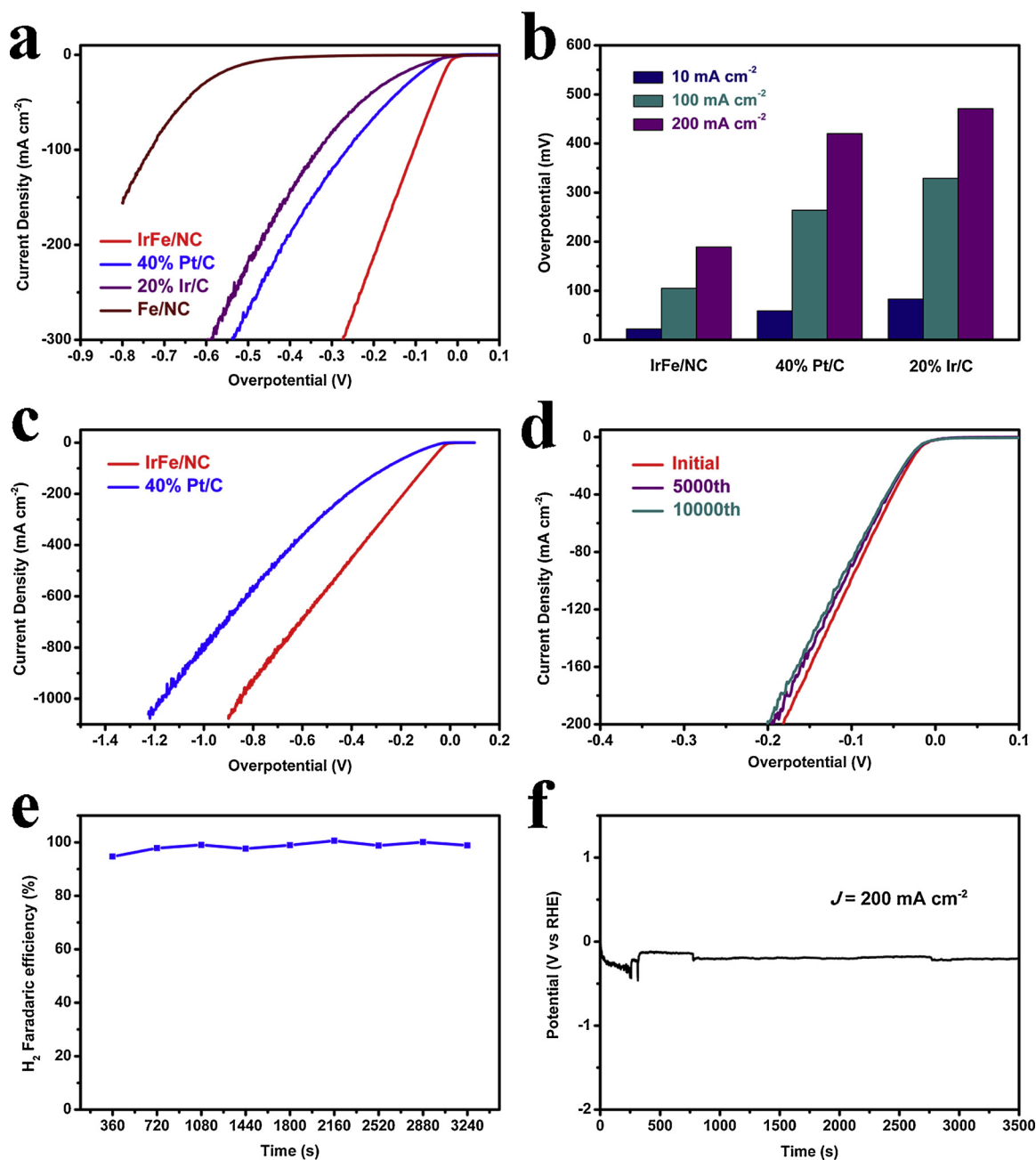


Fig. 4. Electrocatalytic HER performance test of catalysts in 1 M KOH solution. (a) LSV polarization curves of IrFe/NC, Fe/NC, 20% Ir/C and 40% Pt/C with the same mass loading, (b) Summary of overpotential at 10, 100 and 200 mA cm⁻² for IrFe/NC, Ir/C and Pt/C, (c) LSV curves of IrFe/NC and Pt/C catalysts for high current densities (1000 mA cm⁻²), (d) Durability tests for IrFe/NC by means of continuous potential sweeps, (e) Specific Faradaic efficiency for electrochemical production of H₂ measured on IrFe/NC catalyst, (f) Potential required to reach 200 mA cm⁻² for IrFe/NC surveyed by chronopotentiometric method during the Faraday efficiency testing process.

shown in Fig. 6, the largest energy barrier comes from the third step (formation of H₂*), which is considered to be the rate-determining-step (rds) of the overall basic HER. It can be clearly seen that energy barrier reduced in the rds of H₂* formation with the introduction of an iron atom in pure Ir, suggesting that IrFe alloy has better basic HER performance than pure Ir as well.

Taking water adsorption and dissociation into consideration, we supplement some DFT calculations. The diagram of energy profiles along the reaction coordinates for water dissociation is carried out according to the calculation results. As shown in Figure S25, it is an exothermic process for H₂O dissociation on Ir, however it is an endothermic process on Pt, suggesting that H₂O dissociation is highly active on Ir [42]. Thus, IrFe alloy exhibited much higher catalytic

activity in alkaline solution.

In light of the above results, the extraordinary HER performance of IrFe/NC (even at large current densities) relies heavily on the modulated electronic structure accompanied by *d* electron couplings, ultra small alloy nanoparticles, the large density of active sites as well as superior conductivity, to which the layered carbon sheets and interatomic charge polarization can make contributions.

3. Discussion

In summary, electrocatalysts of IrFe alloy supported on N-doped carbon sheets with high activity and durability for HER in basic media at extremely high current densities was synthesized via a facile

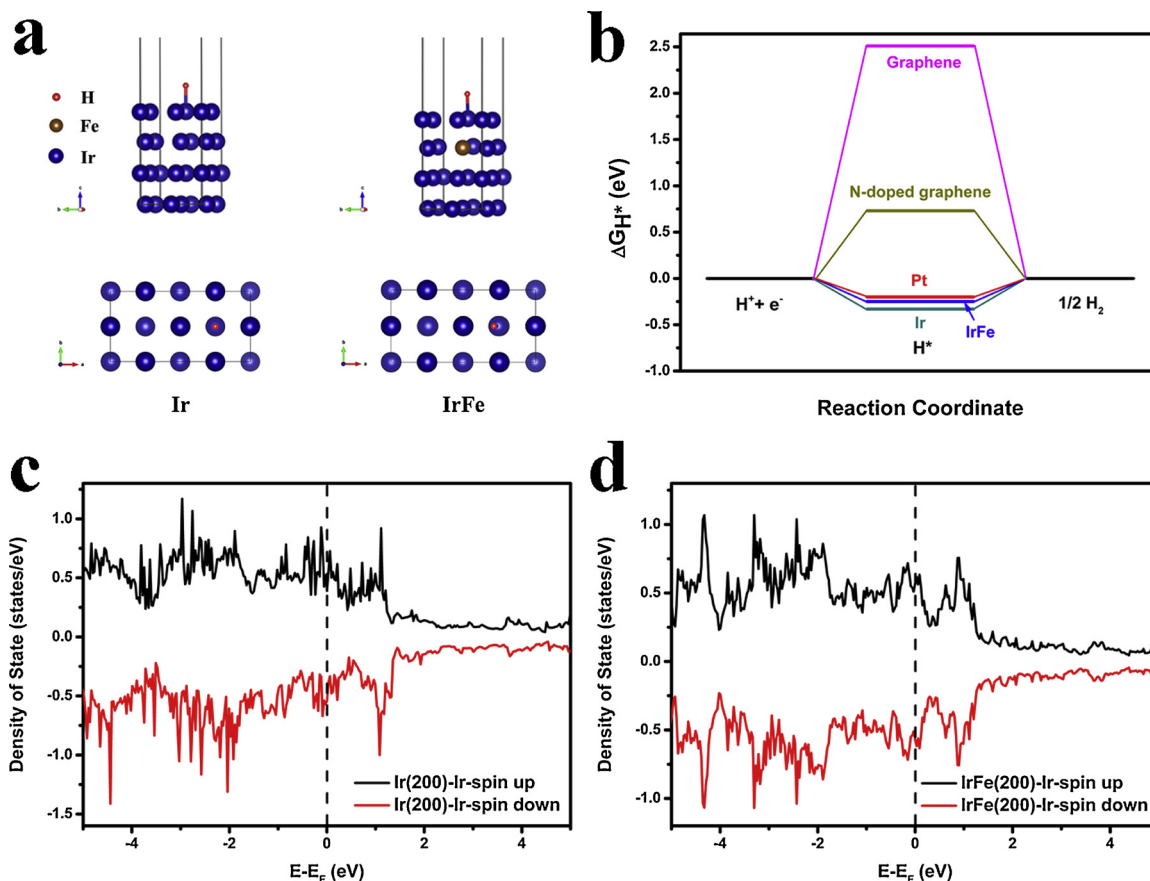


Fig. 5. DFT calculation results of different models. (a) Theoretically optimized atomic models for pure Ir and IrFe, (b) Calculated free-energy diagram of HER at the equilibrium potential for different models, (c, d) Computed PDOS diagrams for Ir atom *d* orbitals in the model of pure Ir (c) and IrFe alloy (d).

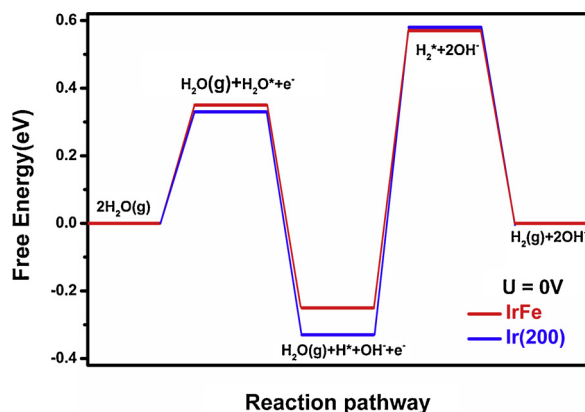


Fig. 6. DFT calculation results of different models. Calculated free-energy diagram of HER at the equilibrium potential for IrFe and Ir under alkaline conditions.

synthetic route. The catalysts require only 850 mV to deliver a huge current density of 1000 mA cm^{-2} , which surpasses all documented electrocatalysts including state-of-the-art commercial noble-metal catalysts Pt/C (1.17 V) in 1 M KOH. Our DFT calculations show that the effective incorporation of foreign TMs would significantly modulates the electronic Fermi level of Ir by electrons transfer owing to the difference in electronegativity. Meanwhile, the regulation of electronic structure of Ir would tune the ΔG_{H^*} near to zero thus significantly improves electrocatalysis activity. This work provided a new insight into the synthesis of advanced catalysts and the development of future alkaline electrolyzers.

Author contributions

P. J. and H. H. contributed equally to this work. Q. C. and P. J. designed and carried out research, analyzed data and wrote the paper. H. H. contributed to theoretical calculation in this paper and wrote the part of calculations. J. D., S. G., S. C., J. L., C. W., Z. S., G. X., K. Y., Y. Y., and L. W. co-wrote the manuscript. All authors discussed the results and commented on the manuscript.

Declaration of Competing Interest

The authors declare that they have no known competing financial interests or personal relationships that could have appeared to influence the work reported in this paper.

Acknowledgements

This study was supported by the National Natural Science Foundation (51772283, 21271163), the Hefei Science Center CAS (No. 2016HSC-IU011), a the National Key R&D Program of China (Grant No. 2016YFA0401801) and Fundamental Research Funds for the Central Universities (WK2060140021). The calculations were completed on the supercomputing system in the Supercomputing Center of USTC. XAFS spectra at the Fe L-edge were recorded at the beamline BL 08U1A station (Shanghai Synchrotron Radiation Facility, SSRF) and the soft X-ray magnetic circular dichroism end station (XMCD) of National Synchrotron Radiation Laboratory (NSRL).

Appendix A. Supplementary data

Supplementary material related to this article can be found, in the

online version, at doi:<https://doi.org/10.1016/j.apcatb.2019.117965>.

References

- [1] M. Gong, W. Zhou, M.C. Tsai, J.G. Zhou, M.Y. Guan, M.C. Lin, B. Zhang, Y.F. Hu, D.Y. Wang, J. Yang, S.J. Pennycook, B.J. Hwang, H.J. Dai, *Nat. Commun.* 5 (2014) 5695.
- [2] T. Zhang, M.Y. Wu, D.Y. Yan, J. Mao, H. Liu, W.B. Hu, X.W. Du, T. Ling, S.Z. Qiao, *Nano Energy* 43 (2018) 103–109.
- [3] X.X. Zou, Y. Zhang, *Chem. Soc. Rev.* 44 (2015) 5148–5180.
- [4] Y.P. Liu, G.T. Yu, G.D. Li, Y.H. Sun, T. Asefa, W. Chen, X.X. Zou, *Angew. Chem. Int. Edit.* 54 (2015) 10752–10757.
- [5] Z.H. Pu, I.S. Amiinu, Z.K. Kou, W.Q. Li, S.C. Mu, *Angew. Chem. Int. Edit.* 56 (2017) 11559–11564.
- [6] H. Lv, X. Chen, D.D. Xu, Y.C. Hu, H.Q. Zheng, S.L. Suib, B. Liu, *Appl. Catal. B: Environ.* 238 (2018) 525–532.
- [7] N.N. Du, C.M. Wang, X.J. Wang, Y. Lin, J. Jiang, Y.J. Xiong, *Adv. Mater.* 28 (2016) 2077–2084.
- [8] L.L. Zhu, H.P. Lin, Y.Y. Li, F. Liao, Y. Lifshitz, M.Q. Sheng, S.T. Lee, M.W. Shao, *Nat. Commun.* 7 (2016) 12272.
- [9] J. Zhang, T. Wang, P. Liu, Z.Q. Liao, S.H. Liu, X.D. Zhuang, M.W. Chen, E. Zschech, X.L. Feng, *Nat. Commun.* 8 (2017) 15437.
- [10] T. Wang, X.J. Wang, Y. Liu, J. Zheng, X.G. Li, *Nano Energy* 22 (2016) 111–119.
- [11] Y.L. Chen, G.T. Yu, W. Chen, Y.P. Liu, G.D. Li, P.W. Zhu, Q. Tao, Q.J. Li, J.W. Liu, X.P. Shen, H. Li, X.R. Huang, D.J. Wang, T. Asefa, X.X. Zou, *J. Am. Chem. Soc.* 139 (2017) 12370–12373.
- [12] J.W. Su, Y. Yang, G.L. Xia, J.T. Chen, P. Jiang, Q.W. Chen, *Nat. Commun.* 8 (2017) 14969.
- [13] F.L. Yang, Y.M. Zhao, Y.S. Du, Y.T. Chen, G.Z. Cheng, S.L. Chen, W. Luo, *Adv. Energy Mater.* (2018) 1703489.
- [14] W.D. Li, Y. Liu, M. Wu, X.L. Feng, S.A.T. Redfern, Y. Shang, X. Yong, T.L. Feng, K.F. Wu, Z.Y. Liu, B.J. Li, Z.M. Chen, J.S. Tse, S.Y. Lu, B. Yang, *Adv. Mater.* (2018) 1800676.
- [15] Z.C. Zhang, G.G. Liu, X.Y. Cui, B. Chen, Y.H. Zhu, Y. Gong, F. Saleem, S.B. Xi, Y.H. Du, A. Borgna, Z.C. Lai, Q.H. Zhang, B. Li, Y. Zong, Y. Han, L. Gu, H. Zhang, *Adv. Mater.* (2018) 1801741.
- [16] Y. Zheng, Y. Jiao, A. Vasileff, S.Z. Qiao, *Angew. Chem. Int. Edit.* 57 (2018) 7568–7579.
- [17] H.Q. Zhou, F. Yu, Q. Zhu, J.Y. Sun, F. Qin, L. Yu, J.M. Bao, Y. Yu, S. Chen, Z.F. Ren, *Energy Environ. Sci.* 11 (2018) 2858–2864.
- [18] Y.C. Pi, N. Zhang, S.J. Guo, J. Guo, X.Q. Huang, *Nano Lett.* 16 (2016) 4424–4430.
- [19] J.R. Feng, F. Lv, W.Y. Zhang, P.H. Li, K. Wang, C. Yang, B. Wang, Y. Yang, J.H. Zhou, F. Lin, G.C. Wang, S.J. Guo, *Adv. Mater.* 29 (2017) 1703798.
- [20] Y.C. Pi, Q. Shao, P.T. Wang, J. Guo, X.Q. Huang, *Adv. Funct. Mater.* 27 (2017) 1700886.
- [21] J. Durst, C. Simon, F. Hasche, H.A. Gasteiger, *J. Electrochem. Soc.* 162 (2015) F190–F203.
- [22] H.B. Wu, B.Y. Xia, L. Yu, X.Y. Yu, X.W. Lou, *Nat. Commun.* 6 (2015) 6512.
- [23] B. You, X. Liu, G.X. Hu, S. Gul, J. Yano, D.E. Jiang, Y.J. Sun, *J. Am. Chem. Soc.* 139 (2017) 12283–12290.
- [24] J. Park, Y.J. Sa, H. Baik, T. Kwon, S.H. Joo, K. Lee, *ACS Nano* 11 (2017) 5500–5509.
- [25] P. Jiang, J.T. Chen, C.L. Wang, K. Yang, S.P. Gong, S. Liu, Z.Y. Lin, M.S. Li, G.L. Xia, Y. Yang, J.W. Su, Q.W. Chen, *Adv. Mater.* 30 (2018) 1705324.
- [26] Y. Yang, Z.Y. Lun, G.L. Xia, F.C. Zheng, M.N. He, Q.W. Chen, *Energy Environ. Sci.* 8 (2015) 3563–3571.
- [27] K. Yang, P. Jiang, J.T. Chen, Q.W. Chen, *ACS Appl. Mater. Interfaces* 9 (2017) 32106–32113.
- [28] H.G. Zhang, S. Hwang, M.Y. Wang, Z.X. Feng, S. Karakalos, L.L. Luo, Z. Qiao, X.H. Xie, C.M. Wang, D. Su, Y.Y. Shao, G. Wu, *J. Am. Chem. Soc.* 139 (2017) 14143–14149.
- [29] Y.J. Chen, S.F. Ji, Y.G. Wang, J.C. Dong, W.X. Chen, Z. Li, R.A. Shen, L.R. Zheng, Z.B. Zhuang, D.S. Wang, Y.D. Li, *Angew. Chem. Int. Edit.* 56 (2017) 6937–6941.
- [30] P.P. Su, H. Xiao, J. Zhao, Y. Yao, Z.G. Shao, C. Li, Q.H. Yang, *Chem. Sci.* 4 (2013) 2941–2946.
- [31] Z.T. Li, H.D. Sun, L.Q. Wei, W.J. Jiang, M.B. Wu, J.S. Hu, *ACS Appl. Mater. Interfaces* 9 (2017) 5272–5278.
- [32] J. Wang, Z.Q. Huang, W. Liu, C.R. Chang, H.L. Tang, Z.J. Li, W.X. Chen, C.J. Jia, T. Yao, S.Q. Wei, Y. Wu, Y.D. Lie, *J. Am. Chem. Soc.* 139 (2017) 17281–17284.
- [33] R. Das, P. Pachfule, R. Banerjee, P. Poddar, *Nanoscale* 4 (2012) 591–599.
- [34] J. Leveque, G.I.N. Waterhouse, J. Kennedy, J.B. Metson, D.R.G. Mitchell, *J. Phys. Chem. C* 115 (2011) 20978–20985.
- [35] F.L. Wang, K. Kusada, D.S. Wu, T. Yamamoto, T. Toriyama, S. Matsumura, Y. Nanba, M. Koyama, H. Kitagawa, *Angew. Chem. Int. Edit.* 57 (2018) 4505–4509.
- [36] Y. Yang, Z.Y. Lin, S.Q. Gao, J.W. Su, Z.Y. Lun, G.L. Xia, J.T. Chen, R.R. Zhang, Q.W. Chen, *ACS Catal.* 7 (2017) 469–479.
- [37] M. Ledendecker, J.S. Mondschein, O. Kasian, S. Geiger, D. Gohl, M. Schalenbach, A. Zeradjanin, S. Cherevko, R.E. Schaak, K. Mayrhofer, *Angew. Chem. Int. Edit.* 56 (2017) 9767–9771.
- [38] N. Danilovic, R. Subbaraman, D. Strmcnik, K.C. Chang, A.P. Paulikas, V.R. Stamenkovic, N.M. Markovic, *Angew. Chem. Int. Edit.* 51 (2012) 12495–12498.
- [39] S.Y. Jing, L.S. Zhang, L. Luo, J.J. Lu, S.B. Yin, P.K. Shen, P. Tsiakaras, *Appl. Catal. B: Environ.* 224 (2018) 533–540.
- [40] S. Gupta, N. Patel, R. Fernandes, R. Kadrekar, A. Dashora, A.K. Yadav, D. Bhattacharyya, S.N. Jha, A. Miotello, D.C. Kothari, *Appl. Catal. B: Environ.* 192 (2016) 126–133.
- [41] J. Greeley, J.K. Norskov, L.A. Kibler, A.M. El-Aziz, D.M. Kolb, *Chemphyschem* 7 (2006) 1032–1035.
- [42] J. Wang, Z.Z. Wei, S.J. Mao, H.R. Li, Y. Wang, *Energy Environ. Sci.* 11 (2018) 800–806.